Composites & nanocomposites

Ultra-high local plasticity in high-strength nanocomposites

Rongmei Niu[1], Ke Han[1,*], Zhaolong Xiang[2], Li Qiao[3], and Theo M. Siegrist[1,4]

[1] *National High Magnetic Field Laboratory, Tallahassee, Florida, USA*
[2] *Northeast University, Shenyang, Liaoning, People's Republic of China*
[3] *Taiyuan University of Science and Technology, Taiyuan City, Shanxi, People's Republic of China*
[4] *FAMU-FSU College of Engineering, Tallahassee, Florida 32310, USA*

ABSTRACT

We subjected an aged Cu-24wt%Ag ingot to cold drawing to create a high-strength nanostructured composite wire with both Cu-rich proeutectic and Ag-rich eutectic components. During the drawing, a fine lamellar structure (average spacing 20 ± 6 nm) developed in the proeutectic component, which contained a high density of Ag fibers (average width below 5 nm) embedded in the matrix. In the eutectic component, a relatively coarse structure developed, with an average Ag grain size around 100 nm. The result of such a bimodal size of Ag fibers was ultra-high bending plasticity, i.e., the drawn wire tolerated 59% bending strain at the outermost edge, 15 times its tensile elongation (3.6%). During our bending test, dynamic recovery and partial recrystallization occurred more near the inner edge than near the outer edge and primarily in the eutectic component. High bending strain caused some of the thicker Ag fibers to become discontinuous and lose their original alignment. This structural evolution increased local plasticity, resulting in an unexpectedly high achievable bending strain, which is unusual in nano-sized, Ag-fiber-reinforced high-strength composites.

Address correspondence to E-mail: han@magnet.fsu.edu

🖄 Springer

GRAPHIC ABSTRACT
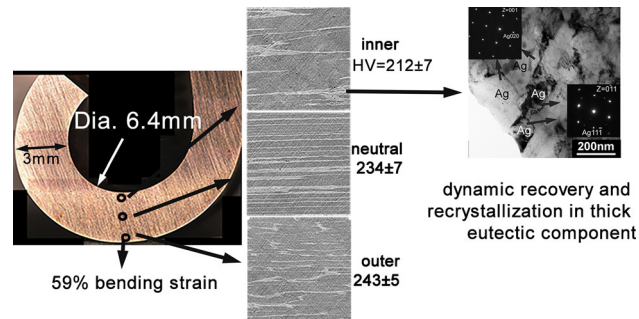
Introduction

The generation of high magnetic fields requires highly conductive magnet-winding materials with high strength to withstand the substantial Lorentz forces acting on the wire [1–6]. Cu-based nanocomposites are excellent candidates for this application, because of their high electrical conductivity and high mechanical strength [7–9]. Heavily cold-drawn CuAg and CuNb nanocomposite wires exhibit higher mechanical strength when compared not only to their bulk constituent metals, but also to the rule-of-mixtures prediction [10–22]. These materials are termed nanocomposites due to the small size of the different phase elements and to the very fine grain size obtained in each phase in the transverse cross-section because of the severe plastic deformation (SPD) [8, 23–36]. The substantially improved mechanical strength stems from the high density of nano-scale fibers, which results in the unique plasticity mechanisms that is not commonly found in bulk materials [10, 37–41].

To achieve high strength with limited electrical conductivity compromise, SPD is an effective approach [14, 42, 43]. SPD techniques such as casting-forging-cold drawing, accumulative drawing and bundling (ADB), accumulative roll bonding (ARB), have been extensively studied in polycrystalline metals and alloys [14, 15, 41, 44–52]. In SPD-processed materials, high defect density is essential for obtaining high strength, but also increases stored energy and driving force for boundary migration, while reducing the thermal stability [29–31, 35, 36].

For instance, incorporating a high density of twin boundaries with spacing of $\sim$ 15 nm in polycrystalline Cu grains, a ten-fold increase in mechanical strength is achieved over coarse-grained Cu [53]. However, the thermal stability of Cu with a high density of nanotwins is low. Nanotwins were reported to recrystallize after long-term storage at room temperature under moderate rolling deformation [54, 55], and high-purity Cu (99.96%) deformed by equal-channel angular extrusion to a high strain was partially recrystallized after long-term storage at room temperature [56]. Researchers observed twins in heavily deformed eutectic Cu–Ag composites [57–59]. Therefore, in heavily cold-drawn nanocomposites, investigation the stability of nano-scaled fibers is significantly important for their application.

Nanocomposite wire winding is a crucial procedure for constructing high field pulsed magnets. Previously [60, 61], we note that the maximum bending strain is almost ten times the tensile elongation for a CuNb wire bent on a 6.4 mm diameter mandrel. Nanocomposite materials produced by the different SPD methods exhibit very high strengths but tensile elongation is often low ($\sim$ 3–4%). Therefore, the conventional tensile elongation cannot be used to predict bending strain.

To predict the bending behavior of nanocomposites, the main challenge is understanding the properties of the high density of nano-scaled fibers. In this work, we have studied the extreme high bending plasticity in the cold-drawn CuAg nanocomposite and the stability of the nano-scale fibers in the wire under extreme deformation.

Materials and methods

Wires fabrication

A Cu-24 wt% Ag (Cu-16 at.% Ag) ingot with a diameter of 50 mm and length of 250 mm was cast by Ames Lab. The ingot was homogenized at 700 °C for 1 h in 1% hydrogen—99% Argon, and subsequently aged at 310 °C for 36 h in 99% Argon. After the heat-treatment, the ingot surface was machined to remove the surface oxidization layer with high porosity. The machined ingot was swaged from 36.8 mm to 31.8 mm in diameter. Subsequently, the swaged rod was gradually cold-drawn to a rectangular profile of 3.0 mm × 6.0 mm. The total drawing true strain of the CuAg wire was 4.1.

Tensile test

Tensile tests of the CuAg wire were performed in accordance with the ASTM E8-93 on an MTS test machine at 295 K in displacement control mode at a rate of 0.5 mm/min, see Fig. 1. A wire extensometer was used to record the applied strain.

Bending test

A Knoop indenter was used to mark the samples for bending strain measurement. An as-drawn wire was
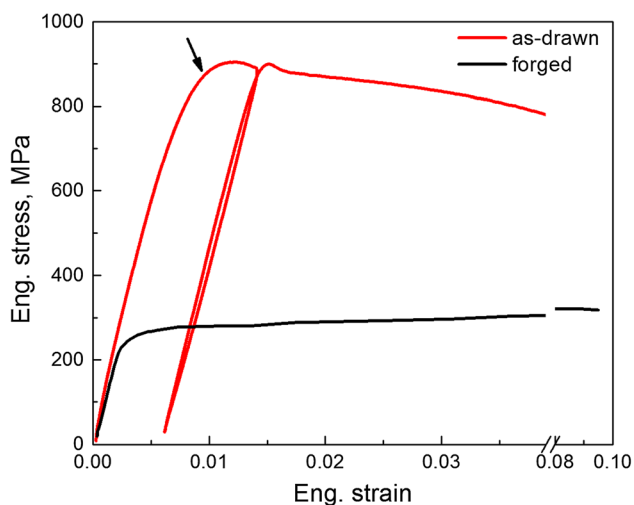

Figure 1 Tensile stress–strain curves of the as-drawn wire and forged rod [10] at room temperature. The rounding part in the stress–strain curve is marked on the as-drawn wire. The stress–strain curve of our as-drawn wire appears more rounded than that of the forged rod after elastic stage [10]. The rounding is related to the low-strain anelasticity in composite materials.

ground and polished on the 3.0 mm-thick side. Subsequently, Knoop indents were made on the polished surface, with the Knoop indenter geometry being an extended pyramid with length to width ratio of 7:1. To understand the influence of the Knoop indent size on the measured strain, we aligned one set of indents (#1, #3, and #4 in Fig. 2a) with their long diagonals parallel to the wire axis and another set (#2 in Fig. 2a) with their long diagonals perpendicular to the wire axis. We used a 6.4 mm-diameter mandrel to bend the wire to angles of 20°, 37°, 56°, 73°, 84°, 107°, 143°, and 173° (taking spring-back into account). We compared the length of the long and short diagonals of each indent before and after bending in order to determine bending strain (see Fig. 2b–d). We then verified the resulting bending strain values by measuring relevant microstructural features near these indents (Fig. 2e and f).

Hardness test

Micro-hardness tests were performed on a Tukon 2100 tester with a Vickers diamond pyramid indenter on the as-drawn and as-bent wires along the 3 mm-thick cross-section with a load of 300 g and a dwell time of 10 s. Six to ten tests were conducted for each measurement.

Microstructure characterization

Scanning electron microscopy (SEM, Zeiss 1540 ESB) was used to measure the Knoop indent size on the wire before and after bending. While SEM was used to observe the morphology evolution of proeutectic and eutectic components.

To prepare TEM samples, small slices ($\sim$ 500 μm thickness x 3 mm width × 4 mm length) with their surface parallel to the 3.0 mm-thick side of the wire were cut from as-drawn and as-bent wires along the wire axis. Two slices from as-bent wires were placed with the maximal tension edge side by side, then glued on a copper ring with the maximal tension edges in the ring centre. Another set of two slices from as-bent wires were placed with the maximal compression edge side by side, then glued on a copper ring with the maximal compression edges in the ring centre. Both the sliced samples from the as-drawn wires and glued samples from the as-bent wires were then ground to $\sim$ 150 μm in thickness. Subsequently, the samples were dimpled and ion milled on a liquid nitrogen stage at $\sim$ 2.5 keV using
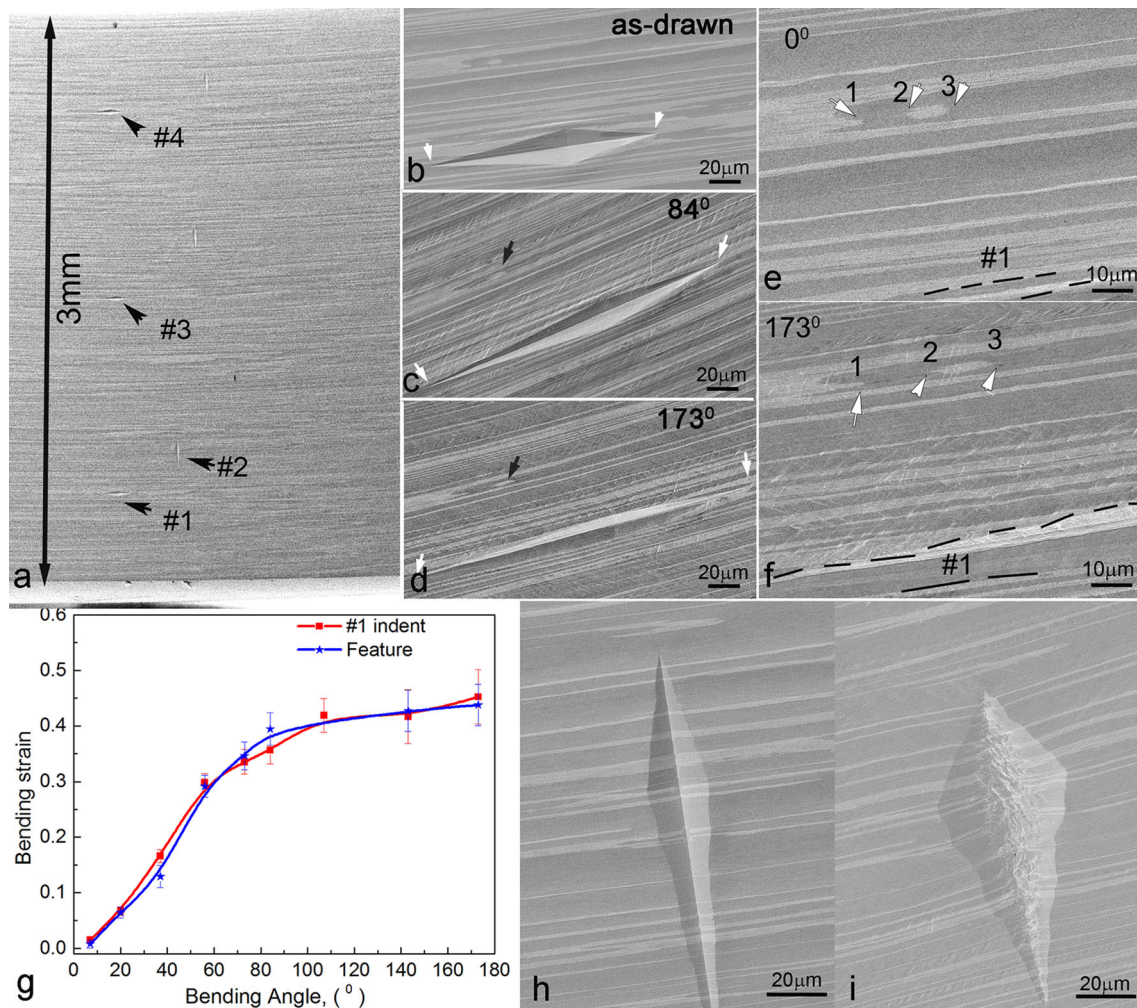
Figure 2 SEM characterization of the bending strain by Knoop indents evolution. **a** distribution of indents across the 3.0 mm side. The indents are marked by #1, #2, #3, and #4. The #1 indent is the closest to the outermost edge. The long and short diagonals of the #1, #3, and #4 indents are parallel to the wire length direction and width, respectively. While the long and short diagonal of #2 indent are perpendicular to wire length direction and width, respectively. **b** to **d** diagonal's evolution of the #1 indent at bending angles of 0°, 84°, and 173°, respectively. The white arrows indicate the long diagonal length. The black arrow indicates an Ag feature nearby. This feature is enlarged in **e** and **f**. By measuring this feature size, or the distance between the labeled numbers in **e** and **f**, the bending strain was determined and compared to that measured by Knoop indent. (Before bending, the average long and short diagonal lengths were 152 ± 4 μm and 22 ± 2 μm, respectively.) **g** plot of the measured true strain from #1 indent and the Ag feature with the bending angle. **h** the #2 indent before bending. **i** a pronounced local plastic deformation at the #2 indent after 173° bending is observed.

an incidence angle of 5°–7°. These TEM samples were examined in a JEOL JEM-ARM 200CF electron microscope operating at 200 kV.

XRD

Standard θ–2θ scans were obtained from the longitudinal cross-sections of as-drawn and as-bent specimens using Cu Kα radiation on a Scintag 2-circle diffractometer.

Model description

The computational periodic cell contains one fcc copper grain with lattice constant 3.632 Å. The CuAg composite was modeled using the Embedded-atom method (EAM) potential [62]. The Ag fiber (approximately 9.23 nm, width × 11.3 nm, thickness) was embedded in the centre of a Cu rectangular prism. The cell dimensions along the x-, y-, and z-directions were approximately 43.1, 29.6, and 31.3 nm,

respectively. The initial composite structure was relaxed via conjugate gradient energy minimization. Figure 7a shows the relaxed configuration of the model, in which the atoms at the perfect fcc sites are shown in green, and the interfaces atoms are made visible as various other colored atoms, i.e., red and white. Visualization of the atoms was done using OVITO [63]. This periodic simulation volume contains approximately 3,211,246 atoms and the relaxed grains contain dislocations at the phase boundaries. The cell volume was oriented with the [11-2] axis along x, the [− 110] axis along y, and the [111] axis along z. Periodic boundary conditions were applied in all three directions.

Computation procedure

A parallel molecular dynamics program, LAMMPS, was used to simulate the behavior of the CuAg composite structure under approximately uniaxial tensile deformation. At the beginning of the simulation and before applying tensile deformation, a Gaussian distribution of the velocities of all the atoms for a specific temperature was generated using a random number generator at a specific temperature. The structure was then deformed by applying a constant tensile engineering strain rate along the x-direction. The other two directions were allowed to shrink to keep the periodic cell volume constant. The simulations were performed in a constant NPT ensemble. Atomic positions, velocities and accelerations were updated at each time step using the Velocity-Verlet algorithm. The total simulation time was set at 160 ps with a time step of 0.001 ps. This short time period resulted in a very high strain rate, inherent to every MD simulation, but was necessary to obtain a significant amount of deformation within a reasonable simulation time. For our simulations, the applied strain rate was 10^{10} s^{-1}. The temperatures of the simulations were controlled using a Nosé–Hoover temperature thermostat set to a constant temperature of 300 K.

Results

Tensile properties

After having first passed through a yielding stage at the beginning of plastic deformation, the wire reached its ultimate tensile strength (UTS) at a level of strain less than 1%. We observed yield strength as high as 891 ± 12 MPa and UTS as high as 903 ± 1 MPa in our as-drawn CuAg wire, indicating strain-hardening effect (Fig. 1). Our wire showed early instability, i.e., it began to "neck" during tensile testing much earlier than the forged rods of similar material previously studied by Han et al. [10]. This instability in our wires, along with their higher yield strength values, meant that, beyond strain of 1%, we were not able to directly observe evidence of significant strain-hardening. The true strain values of elongation and area-in-reduction (Ar) in our wires were $3.6 \pm 0.3\%$ and $14 \pm 5\%$, respectively. Even though the wire remained ductile throughout our tests, such a large difference between these two values demonstrates that local instability must have occurred at relatively low strain.

Tensile tests of our composite wires revealed the presence of low-strain anelasticity, which we had identified in previous work as an indicator of internal stresses [64]. These internal stresses are likely to have resulted from incompatibility between Cu-rich and Ag-rich phases during cold deformation [13].

Bending strain

In the as-bent wire with a bending diameter of 6.4 mm, we measured bending strain at various bending radial planes (see Fig. 2a and Table 1). Tensile strain occurred at the outer edge, compressive strain at the inner. Using the strain measurements (Table 1), we established a relationship between the axial true strain (ε) and the distance from the outermost edge (X). The resulting equation was $\varepsilon = -0.30X + 59\%$, based on an assumption of linear distribution of strain. Using this equation, we extrapolated the value of ε at the outermost edge as 59%, which is much higher than the true strain of the reduction-in-area at fracture ($14\% \pm 5$). Our extrapolated ε values were not symmetric. Compressive strain at the innermost edge was 30%, about 50% of the tensile strain. We calculated that, after bending by an angle of 173°, the neutral plane of 3.0 mm-thick wire was located about 2.0 mm away from the outer edge. In other words, the neutral plane moved 0.5 mm toward the compression side, i.e., 17% of the thickness of our 3.0 mm wire.

Bending strain values measured using the indents with the long diagonal parallel to the wire axis were

Table 1 Indent positions and strains, assuming the outermost edge of bending as starting position

Indents	Unstrained distance from outer edge (μm)	Measured true strain from indents	Extrapolated true strain $Y = -0.30*X + 0.59$
Outer edge	0.0		0.53
#1	0.4	0.45	
#2	0.6	0.77	0.41
#3	1.4	0.22	
#4	2.3	− 0.12	
Inner edge	3.0		− 0.30

confirmed by bending strain values measured using surrounding microstructural features (Fig. 2e–g). This implies that our strain values measured from indents #1, #3, and #4 are representative and that stress concentration is not sufficient to cause any evident local deformations.

By contrast, bending strain value measured using the indents with the long diagonal parallel to the bending radius (e.g., #2 indent in Fig. 2a) was much greater than those measured from nearby microstructural features and was therefore not representative. The reason for this is that highly localized plastic deformation occurred after bending, especially along the short diagonal (Fig. 2h and i), which was twice the original size after bending to an angle of 173°. The short diagonal stretched under bending, whereas the long diagonal was shortened because of the transverse strain due to the Poisson's ratio in this material. The measured strain at indent #2 is 77%, significantly larger than average strain.

Bending strain is not only relative to the distance from the outer edge, but also depends on the bending angle. Figure 2i indicates a two-stage behavior of the #1 indent on the bending strain vs. bending angle. In the first stage ($< \sim 70°$), the true strain increased rapidly to 34%; in the second stage (70°–173°), the true strain increase slowed, and reached 11% only. The strain vs. bending angle curve exhibits a logarithmic function relationship, consistent with the theoretical prediction. According to the solid beam pure bending theory, the bending true strain on the outer edge with respect to the bending angle (α) follows a logarithmic function [65]: $\varepsilon \propto \ln(1 + h\alpha)$, where h is the wire thickness. An important feature of the logarithmic function is the rapid increase as the variable is small, but a very slow increase as the variable becomes large.

According to the beam bending theory, the deformation strain is a function of the distance y from the neutral axis and the radius of curvature $\Upsilon + h/2$ (measured to the neutral axis of the beam) of the longitudinal axis of the element [66], $\varepsilon = y/(\Upsilon + h/2)$, where Υ is the radius of the mandrel, and h is the wire thickness. Consequently, the maximum tensile strain occurs on the outer edge, while the maximum compressive strain occurs on the inner edge where the wire contacts the bending mandrel. Plane strain conditions are assumed to prevail throughout the deformation process. Though the beam pure bending theory is valid only for elastic and inelastic action under the condition that the beam does not twist or buckle, it serves as a reference for estimating the maximum bending capacity. For a wire with thickness h wound into a coil with an inner diameter of 2Υ, the engineering strain can be expressed as: $\varepsilon = h/(2\Upsilon + h)$. The tensile true strain on the outer edge of the coil can be expressed as: $\varepsilon_o = \ln[1 + h/(2\Upsilon + h)]$ [60], and the compressive strain on the inner edge as: $\varepsilon_i = \ln[1 - h/(2\Upsilon + h)]$. With a wire thickness of 3 mm and mandrel diameter of 6.4 mm, both our calculated engineering strain values at the outer and inner edges were identical, with a value of 32%, based on the assumption that the neutral axis was at half the wire thickness. The true strain values at the outermost and innermost edges were calculated to be 28% and − 39%, respectively. By contrast, the outermost bending strain extrapolated from the Knoops indent was 59%, which was higher than that estimated by the pure bending theory.

For metals, the elastic limit is usually very small, < 0.02%. Considering the limit of beam pure bending theory, researchers developed an empirical equation to estimate the minimum bending diameter (2Υ) using area-in-reduction (Ar) for bars under plastic deformation: $2\Upsilon = (60/(Ar * 100) - 1) * h$,

where h is the bar thickness [65]. For a 3 mm-thick wires with an Ar of 14%, the minimum bending diameter is estimated at 19.8 mm. We were able to bend our wire, however, to a much smaller diameter of 6.4 mm, demonstrating that we achieved ultrahigh bending strain in our nanocomposite. This ultrahigh bending strain exceeds not only the one estimated from the pure bending theory but also the value derived from the empirical relationship.

Location-dependent hardness distribution

Microhardness on the as-bent wire demonstrated that, after an angle of 173° bending, hardness around the neutral plane (234 ± 7) was similar to that of the wire before bending (235 ± 5), Fig. 3. The hardness near the wire outer edge (i.e., tension side) was hardened by 3% to 243 ± 5. In contrast, hardness near the wire inner edge (i.e., compression side) was softened by 10% to 212 ± 7. The hardness evolution after bending implies location-dependent strain-hardening behavior, i.e., work-hardening took place on the outer edge while work softening occurred on the inner edge.

Structure evolution near outer and inner bent edges

After aging heat-treatment at 310 °C, some Ag phases presented as precipitates (∼ 10 nm) in the Cu-rich proeutectic component, others formed the Ag-rich eutectic component (micron-scale) in the ingot [10]. Through the cold drawing, all the elements became fine and aligned along the wire drawing direction. In the as-drawn wire, the Ag-rich eutectic component was lamellar-like embedded between original proeutectic Cu dendrites along the drawing direction, as seen in SEM images. The eutectic component appeared aligned along the wire axis. After bending, the material near the outer edge underwent tension. The eutectic component was observed to become finer and break to short pieces under a certain extended bending strain (Fig. 3b). Parts of the eutectic component became curved, and lost the

Figure 3 Hardness and microstructure in the as-bent wire. **a** micro-hardness distribution on a cross-section of the as-bent wire (3 mm side). The hardness values of the as-bent wire are 243 ± 5 near the outer edge, 234 ± 7 near the neutral plane, and 212 ± 7 near the inner edge. The hardness of the unbent part is 235 ± 5 in the straight wire area. **b** outer edge: discontinuous Ag-rich eutectic component (light contrast) after bending deformation, dark contrast area is the Cu-rich proeutectic component. **c** the neutral plane: eutectic component is continuous and well align to the wire axis. **d** inner edge: coarse and discontinuous eutectic component under compression.
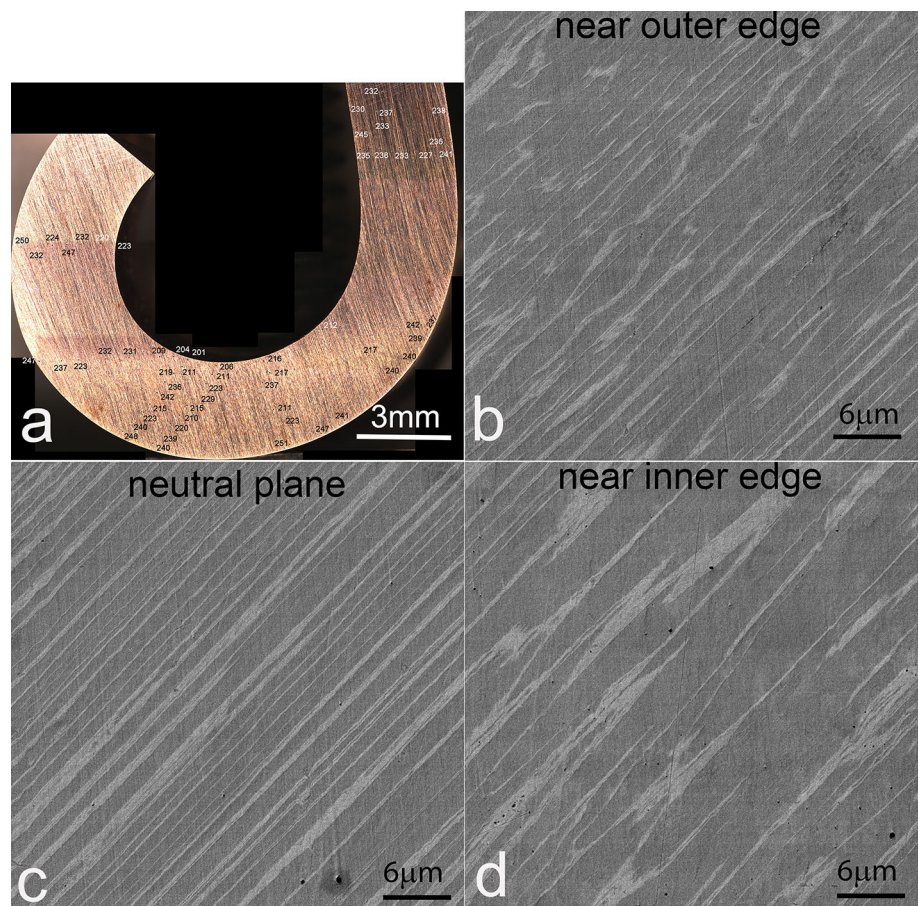
original alignment feature. The component spacing near the outer edge became narrow at some locations, with an average spacing of 1.5 ± 0.2 μm near the outer edge. Near the neutral plane, the eutectic component remained continuous and well aligned with the wire axis (Fig. 3c), with an average eutectic component spacing of $\sim 1.9 \pm 0.3$ μm. The eutectic component became coarse and discontinuous under compression (Fig. 3d), and the average spacing increased to 2.1 ± 0.5 μm near the inner edge of the bending wire.

X-ray characterization

To understand the evolution of the microstructure with respect to the drawing strain, XRD was carried out on both as-drawn and as-bent wires. In the as-drawn wire, the intensities of both (111) and (220) peaks were stronger than the rest (Fig. 4). After bending deformation, the intensity of the (200) reflection was higher than before deformation, and the Full Widths at Half Maximum (FWHM) was lower. Previous research has indicated that residual stress and strain often coexist in as-drawn Cu-Ag composites [64]. We chose the Williamson-Hall (WH) formula to analyze grain sizes, and we took into consideration the dependence of peak broadening on both residual strain and crystallite size (See "Appendix".). The average grain size was 27 ± 6 nm in our as-drawn wire and 50 ± 10 nm in our as-bent
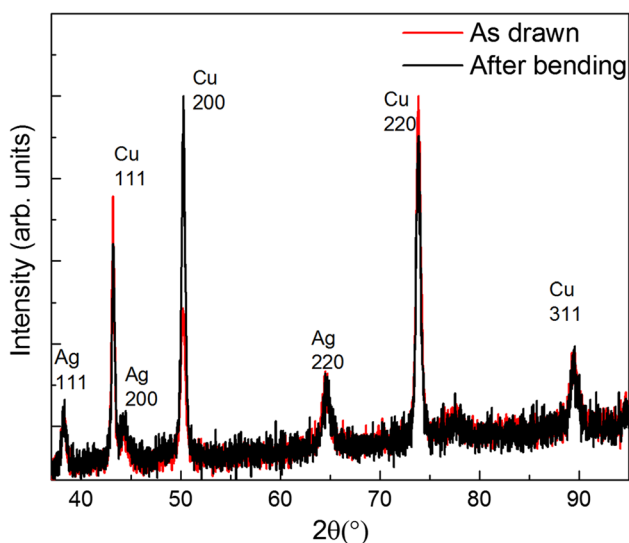

Figure 4 XRD pattern comparison of the structure evolution with the bending deformation. The intensity of (200) became stronger and sharper after the wire bending.

wires. This indicated that grain growth occurred after bending deformation, thus causing a 10% decrease in hardness (from 235 ± 5 to 212 ± 7) at the inner edge of the bent wire (Fig. 3).

Dynamic recovery and recrystallization

SEM observation in Fig. 3 discovered the break and coarsening of Ag-rich eutectic component. To reveal the deformation mechanism, and understand the thick Ag fibers morphology evolution, transmission electron microscopy (TEM) was conducted. TEM observations exhibited a bimodal distribution of Ag fibers in the as-drawn wire: thin fibers in the proeuctectic component (the fine lines in Fig. 5a and b, and the faint lines in Fig. 5c) and thick ones in the eutectic one (marked "Ag" in Fig. 5c). Silver fibers in the proeutectic component were fine and embedded in Cu matrix forming a lamellar structure parallel to the drawing direction. Their size varied from a couple of atomic layers thickness to ~ 5 nm (Fig. 5a and b). The Cu lamellar width was between 6 and 27 nm, with an average of 20 ± 6 nm. Each lamella was often a single grain within the grain. The lamellae had almost an infinite length, and no boundaries intersected the lamella interfaces. By contrast, Ag fibers in the eutectic component had a coarser structure than in the proeutectic component, corresponding to the light contrast in Fig. 3. Most eutectic lamellae were subdivided by elongated Ag and Cu grains with dislocation tangles (Fig. 5c). The lamellar width was approximately 100 nm. Interconnecting boundaries between the lamellae typically were low angle grain boundaries.

In the vicinity of the outer edge in the as-bent wire, the microstructure of the eutectic and proeutectic components evolved differently. In the proeuctectic component, the lamellar structure remained in most of the area. The lamella width, however, was reduced by 25% to 15 ± 4 nm (Fig. 6a). Only a few Cu grains with an average size of 200 nm were observed in proeutectic component (Fig. 6b) implying recrystallization initiation. In these recrystallized Cu grains, most Ag presented as precipitates rather than as solid solutes in the Cu matrix (see the selected area diffracted pattern (SADP) in Fig. 6b inset). Under the extreme high bending deformation strain, Ag fibers may be broken and spheroidized to reduce the interface energy [68]. With diminished grain
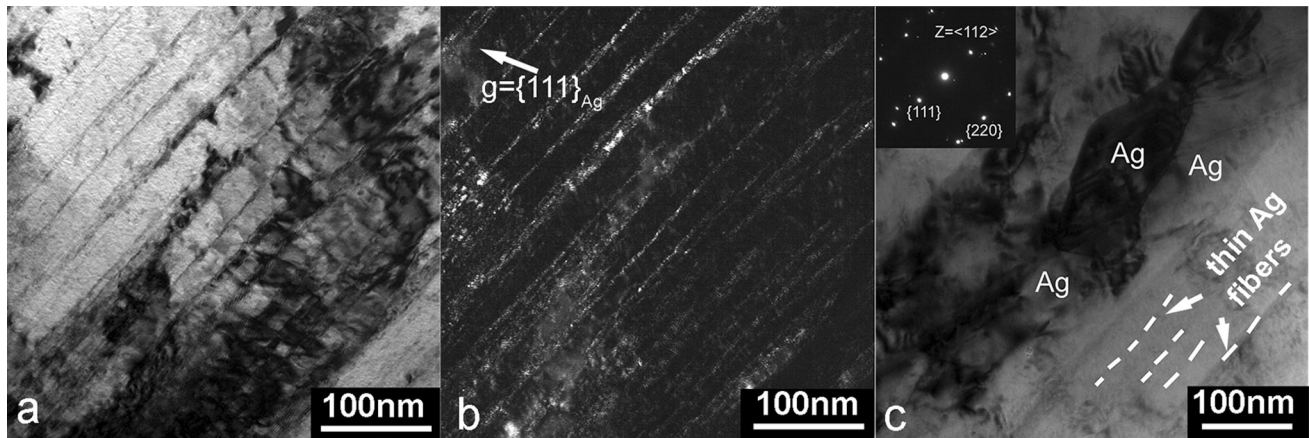
Figure 5 TEM observation of the microstructure in the as-drawn wire. **a** bright field image showing the Cu/Ag lamellar structure in the proeutectic component with Zone axis close to < 011 > . **b** dark field image from the same region in **a** showing the {111} Ag fibers. **c** evident strain field around Ag-rich eutectic component. Dislocations were observed at the Cu/Ag interfaces. The inset indicates no cube-on-cube orientation relationship between Cu and Ag phase in eutectic region, consistent with Han et al.'s previous work [10]. This is, however, different from previous observed results in lamellar eutectic composites [47, 57–59, 67]. The dash lines represents the fine Ag fibers in the proeutectic component. The poor contrast in the proeutectic component is the result of the orientation difference between the proeutectic and eutectic components.

boundary pinning by Ag fibers, grain boundary migration occurred in the Cu lamellae.

In the eutectic component, lamellar boundaries were connected by triple junctions ("*A*" area Fig. 6c), dividing the lamellae into elongated grains. Most Ag grains were larger than Cu grains, but retained a width of 100 nm. Under a different tilting view in TEM, both Ag and Cu grains appeared free of dislocation tangles, which were present before bending. The Ag grains exhibited obvious boundary migration within lamellae (Cf. the Ag grain morphology in Fig. 6c and d), which may be related to the triple junction motion in lamellae. The above observations suggested dynamic recovery and grain boundary migration.

Compared to the outer edge, the inner edge region demonstrated more dynamic recovery and recrystallization in the proeutectic and eutectic components. The recrystallized proeutectic component exhibited submicron-scale recrystallized Cu grains, with a size of 100–200 nm (Fig. 6e). The weak Ag spots in the SADP indicated that Ag precipitates formed as a separated phase (Fig. 6e inset). In the eutectic component, recrystallized Ag grains with a size of 200–300 nm replaced the original elongated grains (Fig. 6f). The SADP revealed no Cu precipitates in Ag grains (Fig. 6f).

MD Simulation

Molecular dynamics (MD) simulation demonstrated that the relaxed composite was free of dislocations in both Cu and Ag grains, while some misfit dislocations remained at the Cu/Ag interfaces (Fig. 7a). As the tensile deformation proceeded, dislocations began to propagate into the Ag and then burst into both the Ag core and the Cu matrix (Fig. 7b). As the dislocation density increased, dislocation started to pile up against the Cu/Ag interfaces, reaching a maximum density value at a strain of 0.1, and saturated with further strain. The dislocation density at a strain of 0.1 and 0.3 (Fig. 7c) showed no evident difference, and therefore it became saturated, while at a strain above 0.4 (Fig. 7d), the dislocation density began to drop. At the same time, some dislocation-free zones started to appear. These simulation results are consistent with our experimental observation, i.e., dynamic recovery takes place under high strain, which in turn assists the progress of further deformation. CuAg nanocomposites are able to endure 0.4 strain without failure.

Figure 6 TEM images from the outer edge **a**–**d** and inner edge **e**–**f** of the as-bent wire. **a** the Cu/Ag lamellar structure in the proeutectic component with Zone axis close to $< 011 >$. The inset indicated the well maintained cube-on-cube orientation relationship of $< 110 >_{Ag}$// $< 110 >_{Cu}$ and $\{111\}_{Ag}$ // $\{111\}_{Cu}$ in Cu matrix. **b** recrystallized Cu grains in the proeutectic component. The areas marked with two circles is the selected regions for the diffraction patterns in the insets. Distinct Ag spots indicate the existence of Ag precipitates. **c** wide lamellar structure in Ag-rich eutectic component. The lamellar boundaries are connected by triple junctions, marked "A". A selected area diffraction pattern (SADP, inset) served to identify the Cu or Ag phases. **d** grain 1 appears coarser than both the grains 2 and 3. The grains 2 and 3 have the same strain and misorientation contrast. Therefore, the grain 1 may have grown toward the grains two and three to reduce the total interface energy. The boundary (black arrows) may migrate toward the grains 2 and 3. **e** Cu-rich recrystallized grains in the proeutectic component under compression. **f** recrystallized Ag grains with sizes of 200–300 nm.
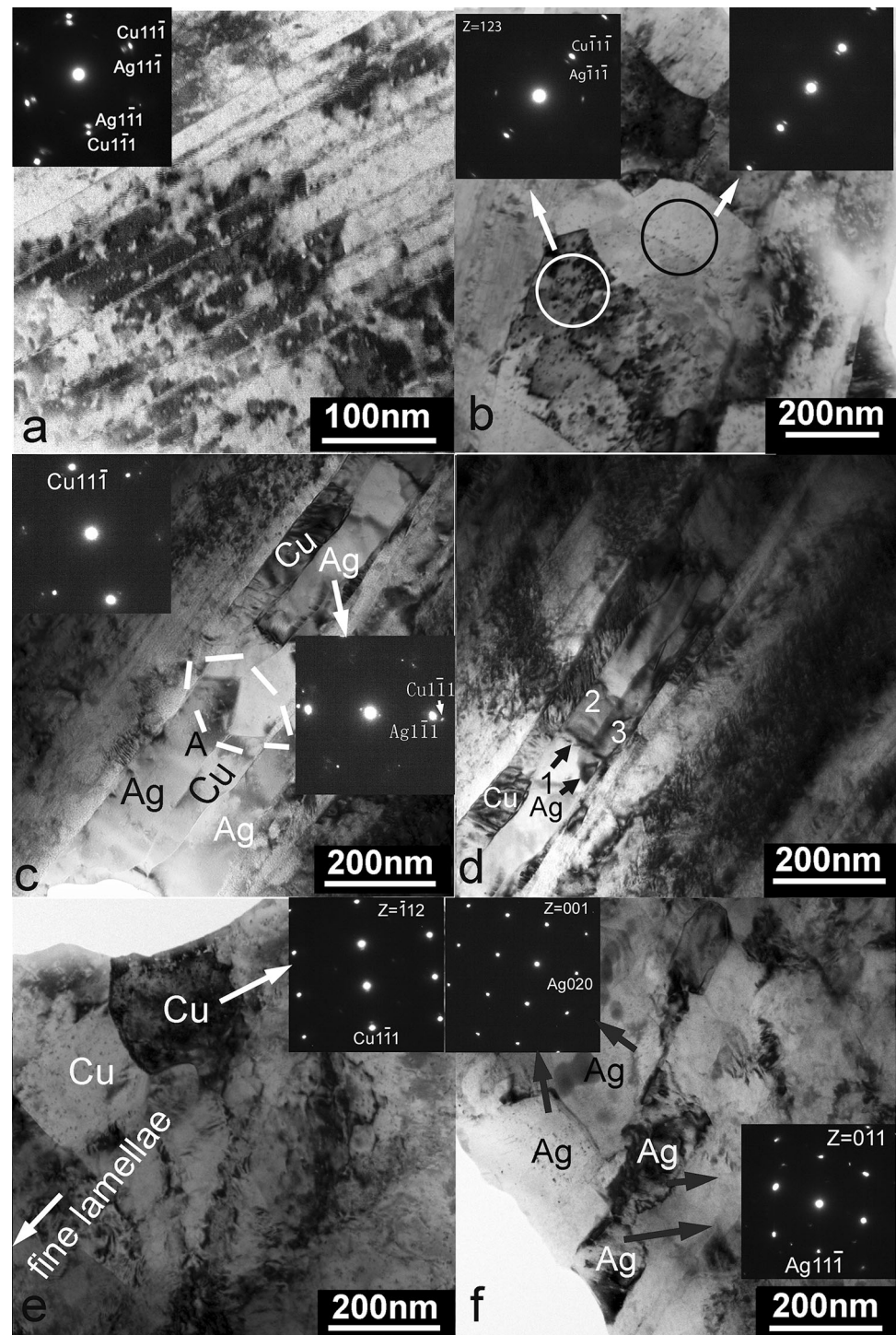

Discussion

Based on our SEM and TEM observations, we believed that the microstructure evolution (Fig. 3b and d) near the outer edges was a combined result of work-hardening, dynamic recovery, and dynamic recrystallization. The close elastic constants of Cu and Ag (in particular their shear moduli) [69] and their cube-on-cube orientation relationship gave rise to co-deformation compatibility in the proeutectic component under tension strain during bending and the conservation of the initial geometry of the reinforcing

Figure 7 MD simulation of CuAg composite at various strains. **a** relaxed configuration of the computational periodic cell showing dislocations at Cu/Ag interfaces. Dislocation distribution at a strain of 0.1 (**b**), 0.3 (**c**), and 0.4 (**d**). Dislocation density at strains of 0.1 and 0.3 remains the same, and is reduced at a strain of 0.4. Some areas free of defects gradually appear with a strain above 0.3, indicated by the arrows in (**c**) and (**d**).
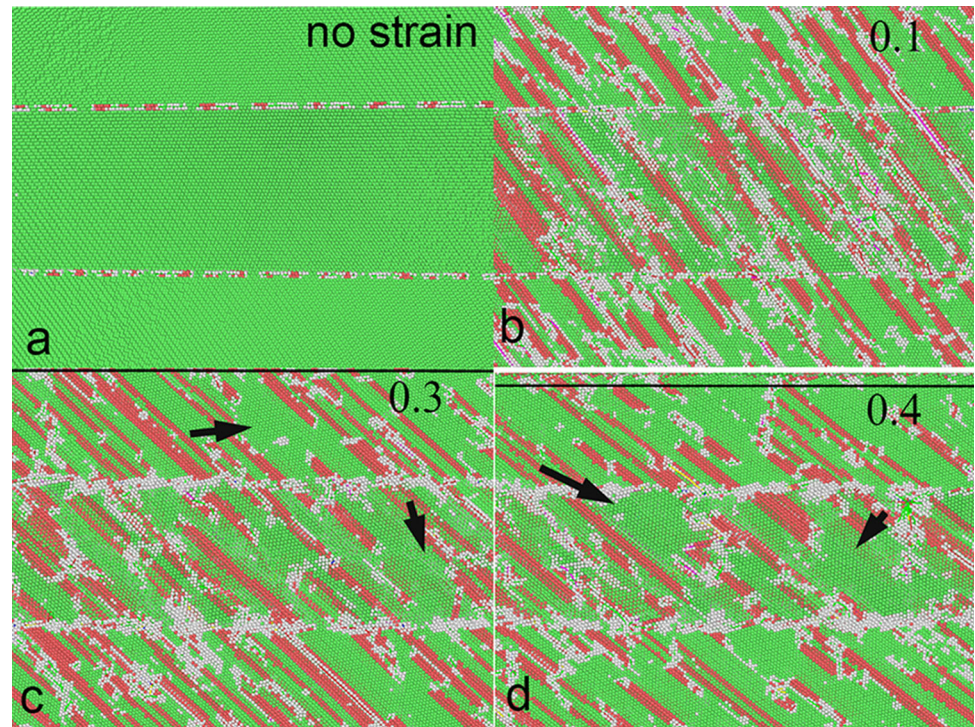
phase. Since dislocations were difficult to accumulate at interfaces, Ag precipitates evolved into Ag nanofibers. Reduced lamellar spacing contributed to the increased hardness (Fig. 3a). The strength difference between the yield strength and the ultimate tensile strength confirmed the work-hardening behavior in our wire as well.

However, in the Ag-rich eutectic component, the large Ag and Cu phases often showed no cube-on-cube orientation relationship (see inset in Fig. 5c). Therefore, the bending deformation was not compatible between the Ag and Cu phases [1], leading to a large residual strain in the eutectic component. Excessive stored energy in the system eventually triggered the initiation of dynamic recovery and recrystallization in the eutectic component, where alignment was lost (see Fig. 3b and d). This results in softening. Because of the low volume fraction of the eutectic component, the softening was counteracted by the work hardening that resulted from the structure refinement near the outer edge.

Near the inner edge, both the lamellar spacing (in the proeutectic component) and the grain sizes (in the eutectic component) increased during bending, providing more space for storing energy as dislocations. Researchers have observed significantly enhanced interface diffusion in nanostructured materials produced by different SPD routes with respect to those in coarse-grained samples [70–72]. Such enhancements were related to their deformed state due to the increased number of dislocations located at the boundaries [72]. Consequently, both dislocation diffusion and interface diffusion contributed to the structure stability. By contrast, near the outer edge, the microstructure of the proeutectic component, with its closely spaced interfaces, was too fine to maintain a stable internal dislocation structure. These phase interfaces acted as a barrier against dynamic recovery and recrystallization. This explains why more of the dynamic recovery and recrystallization occurred near the inner rather than the outer edge. Because the recovered and recrystallized grains were small (~ 200 nm) near the inner edge, hardness there decreased by 10%.

Furthermore, higher Ag content in the eutectic component was another factor for the eutectic component being a favorite site to initiate dynamic recovery and/or recrystallization, since Ag has a lower recrystallization temperature than Cu [73–75].

Hoffman et al. [76] found, in high purity Ag, the absolute grain boundary diffusion coefficients fit the equation, $D_B = 3 \times 10^{-6} e^{(-20200/RT)}$ m^2 s^{-1}, where R is the gas constant, 1.987 cal mol^{-1} K^{-1}, T is the temperature. K. Sommer determined the dislocation

diffusion coefficient was lower by a factor of 5–10 than the boundary diffusion in the temperature range of 353-455 K [77]. Using 1-dimensional diffusion, $d = \sqrt{Dt}$ (where D is the diffusion coefficient and t is the diffusion time), we estimated diffusion distance. The bending time in this work was approximately 5 min in order to avoid a large temperature increase. Our estimation of D_B indicated that the diffusion distance length for Ag at room temperature was approximately 2 nm in a $\sim$ 100 nm Ag grain, and 0.9 nm in an average $\sim$ 20 nm-wide lamella. This implied that, at room temperature, the migration distance of Ag (via boundary and dislocation diffusion) was limited both in the boundary- and dislocation-rich eutectic component and in the interface-rich proeutectic component.

Apparently, a temperature increase accelerated the dominant interfacial diffusion in proeutectic component. If the temperature reached 363 K in the material, the diffusion distance increases to 25 nm in the proeutectic component, exceeding their average lamella width (20 ± 6 nm). If the temperature reached 383 K, the diffusion distance increases to 52 nm, accordingly. The break and spheroidization of Ag fiber showed in Fig. 6b suggested that the temperature rise induced by the bending strain should have been above 363 K, which was also consistent with the experimental observation in Hong's work [78, 79].

It was worth noting that with a decrease of the fine lamellar width to below 10 nm, the volume diffusion kinetics cannot be neglected. Schumacher et al. [24] reported diffusion coefficients: 0.3×10^{-18}, 3.1×10^{-18} and 1.2×10^{-17} for the diffusion of Ag in nanocrystalline Cu at 303 K (30 °C), 353 K (80 °C), and 373 K (100 °C), respectively. The values of corresponding diffusion distance of Ag in proeutectic component were estimated to be 9 nm, 30 nm, and 60 nm. This estimation demonstrated that the interface diffusion significantly impacted the lamellae stability in the heavily drawn CuAg composite with lamella spacing below 10 nm. Slight temperature increases or higher deformation strain in the material would therefore lead to recovery and recrystallization in our composite.

Conclusion

In our cold-deformed and high-strength CuAg wire, we achieved ultra-high bending plasticity–up to 59% bending strain on the outermost edge, a value that exceeded both the tensile elongation (3.6%) and the area-in-reduction at fracture (14%) of this wire. This ultra-high plasticity allowed us to bend a 3 mm-thick wire into a diameter as small as 6.4 mm without causing instability. The high bending strain induced dynamic recovery and recrystallization in this wire, especially in the Ag-rich eutectic component. Thick Ag fibers in the eutectic component became finer in the tensile region and coarser in the compressive region. Dynamic recovery and recrystallization occurred more frequently in the compressive region than in the tensile region. In the proeutectic component, most of the thin Ag fibers remained thin and most of the fine lamellar spacing remained fine. The presence of fine matrix lamellae contributed to high hardness, which indicates high strength. Meanwhile, dynamic recovery and recrystallization produced ultra-high bending plasticity.

Acknowledgments

Compliance with ethical standards

Conflict of interest The authors declare that they have no conflict of interest.

Data and materials availability All data needed to evaluate the conclusions in the paper are present in the paper. Additional data related to this paper may be requested from the authors.

Appendix

Peak broadening due to crystallite size, β_L, was calculated using Debye–Scherrer's formula:

$$\beta_L = K \times \lambda/(\text{size} \times \cos\theta) \tag{1}$$

where θ is the Bragg angle, K is the Scherrer constant (0.9 for integral breath of spherical crystals with cubic symmetry), λ is the wavelength of Cu k_α radiation.

The strain induced broadening, β_s, due to crystal imperfection and distortion was calculated using the formula:

$$\beta_s = 4 \times \text{strain} \times \sin/\cos \tag{2}$$

Williamson-Hall (W-H) analysis is a simplified integral breadth method where both size-induced and strain-induced broadening were deconvoluted by considering the peak width as a function of 2θ [80, 81]:

$$\begin{aligned}\beta_{tot} &= \beta_L + \beta_S \\ &= K \times \lambda/(\text{size} \times \cos) + 4 \times \text{strain} \times \sin\theta/\cos\end{aligned} \tag{3}$$

where β_{tot} is total peak broadening. By rearranging the above equation, we got

$$\beta_{tot} \times \cos\theta = K \times \lambda/\text{size} + 4 \times \text{strain} \times \sin\theta \tag{4}$$

Comparing Eq. 4 to the standard equation for a straight line ($y = c + mx$, c = intercept; m = slope), we obtained the size component from the intercept ($K\lambda/\text{size}$) and the strain component from the slope ($4 \times \text{strain}$) by plotting $\beta_{tot}\cos\theta$ versus $\sin\theta$.

References

[1] Bacon JL, Ammerman CN, Coe H, Ellis GW, Lesch BL, Sims JR, Schillig JB, Swenson CA (2002) The U.S. NHMFL 100 Tesla multi-shot magnet. IEEE Trans Appl Supercond 12(1):695–698. https://doi.org/10.1109/TASC.2002.1018496

[2] Marshall WS, Swenson CA, Gavrilin A, Schneider-Muntau HJ (2004) Development of "Fast Cool" pulse magnet coil technology at NHMFL. Phys. B 346–347:594–598. https://doi.org/10.1016/j.physb.2004.01.156

[3] Marshall WS, Swenson CA, Gavrilin AV, Rickel DG, Schneider-Muntau HJ (2004) Development of 'poly-layer' assembly technology for pulsed magnets. IEEE Trans Appl Supercond 14(2):1241–1244. https://doi.org/10.1109/TASC.2004.830542

[4] Schneider-Muntau HJ, Ke H, Bednar NA, Swenson CA, Walsh R (2004) Materials for 100 T monocoil magnets. IEEE Trans Appl Supercond 14(2):1153–1156. https://doi.org/10.1109/TASC.2004.830461

[5] Swenson CA, Marshall WS, Gavrilin AV, Han K, Schillig J, Sims JR, Schneider-Muntau HJ (2004) Progress of the insert coil for the US-NHMFL 100T multi-shot pulse magnet. Phys B 346–347:561–565. https://doi.org/10.1016/j.physb.2004.01.082

[6] Swenson CA, Marshall WS, Miller EL, Pickard KW, Gavrilin AV, Han K, Schneider-Muntau HJ (2004) Pulse magnet development program at NHMFL. IEEE Trans Appl Supercond 14(2):1233–1236. https://doi.org/10.1109/TASC.2004.830538

[7] Embury J, Han K (2004) A survey of processing methods for high strength-high conductivity wires for high field magnet applications. In: megagauss magnetic field generation, its application to science and ultra-high pulsed-power technology. pp 147-153. https://doi.org/10.1142/9789812702517_0026

[8] Embury J, Han K, Sims J, Coulter J, Pantsyrnyi V, Shikov A, Bochvar A (2004) Fabrication routes for high strength-high conductivity wires. In: megagauss magnetic field generation, its application to science and ultra-high pulsed-power technology. pp 158–160. https://doi.org/10.1109/TASC.2004.830538

[9] Embury JD, Han K (1998) Conductor materials for high field magnets. Curr Opin Solid State Mater Sci 3(3):304–308. https://doi.org/10.1016/S1359-0286(98)80106-X

[10] Han K, Vasquez AA, Xin Y, Kalu PN (2003) Microstructure and tensile properties of nanostructured Cu-25wt%Ag. Acta Mater 51(3):767–780. https://doi.org/10.1016/S1359-6454(02)00468-8

[11] Sakai Y, Schneider-Muntau HJ (1997) Ultra-high strength, high conductivity Cu-Ag alloy wires. Acta Mater 45(3):1017–1023. https://doi.org/10.1016/S1359-6454(96)00248-0

[12] Thilly L, Lecouturier F, Coffe G, Peyrade JP, Askenazy S (2000) Ultra high strength nanocomposite conductors for pulsed magnet windings. IEEE Trans Appl Supercond 10(1):1269–1272. https://doi.org/10.1109/77.828466

[13] Han K, Embury JD, Sims JR, Campbell LJ, Schneider-Muntau HJ, Pantsyrnyi VI, Shikov A, Nikulin A, Vorobieva A (1999) The fabrication, properties and microstructure of Cu–Ag and Cu–Nb composite conductors. Mater Sci Eng, A 267(1):99–114. https://doi.org/10.1016/S0921-5093(99)00025-8

[14] Mara NA, Beyerlein IJ (2015) Interface-dominant multilayers fabricated by severe plastic deformation: Stability under extreme conditions. Curr Opin Solid State Mater Sci 19(5):265–276. https://doi.org/10.1016/j.cossms.2015.04.002

[15] Mara NA, Beyerlein IJ (2014) Review: effect of bimetal interface structure on the mechanical behavior of Cu–Nb

fcc–bcc nanolayered composites. J Mater Sci 49(19):6497–6516. https://doi.org/10.1007/s10853-014-8342-9

[16] Mara NA, Bhattacharyya D, Dickerson PO, Hoagland RG, Misra A (2010) Ultrahigh strength and ductility of Cu-Nb nanolayered composites. Mater Sci Forum 633–634:647–653. https://doi.org/10.4028/www.scientific.net/MSF.633-634.647

[17] Tian YZ, Zhang ZF (2009) Microstructures and tensile deformation behavior of Cu–16wt.%Ag binary alloy. Mater Sci Eng A 508(1):209–213. https://doi.org/10.1016/j.msea.2008.12.050

[18] Tian YZ, Zhang ZF, Wang ZG (2009) Cyclic deformation and fatigue cracking behaviors of Cu–28wt%Ag binary alloy. Phil Mag 89(21):1715–1730. https://doi.org/10.1080/14786430903032548

[19] Wang CJ, Ning YT, Zhang KH, Geng YH, Bi J, Zhang JM (2009) Thermal stability of heavily deformed Ag–10wt.%Cu microcomposite wires. Mater Sci Eng A 517(1):219–224. https://doi.org/10.1016/j.msea.2009.03.065

[20] Wu ZW, Liu JJ, Chen Y, Meng L (2009) Microstructure, mechanical properties and electrical conductivity of Cu–12wt.% Fe microcomposite annealed at different temperatures. J Alloys Compd 467(1):213–218. https://doi.org/10.1016/j.jallcom.2007.12.020

[21] Zhang L, Meng L (2004) Microstructure, mechanical properties and electrical conductivity of Cu–12 wt.% Ag wires annealed at different temperature. Mater Lett 58(30):3888–3892. https://doi.org/10.1016/j.matlet.2004.08.014

[22] Zhang L, Meng L (2005) Evolution of microstructure and electrical resistivity of Cu–12wt.%Ag filamentary microcomposite with drawing deformation. Scripta Mater 52(12):1187–1191. https://doi.org/10.1016/j.scriptamat.2005.03.016

[23] Han K, Embury J, Sims J, Pantsyrnyi V, Shikov A, Bochvar A (1998) Fabrication routes for high strength high conductivity wires. Los Alamos National Lab., NM. https://doi.org/10.1016/S0921-5093(99)00025-8

[24] Sakai Y, Inoue K, Maeda H (1994) High-strength and high-conductivity Cu-Ag alloy sheets: new promising conductor for high-field Bitter coils. IEEE Trans Magn 30(4):2114–2117. https://doi.org/10.1109/20.305687

[25] Sakai Y, Inoue K, Asano T, Maeda H (1992) Development of a high strength, high conductivity copper-silver alloy for pulsed magnets. IEEE Trans Magn 28(1):888–891. https://doi.org/10.1109/20.120021

[26] Davy CA, Han K, Kalu PN, Bole ST (2008) Examinations of Cu-Ag composite conductors in sheet forms. IEEE Trans Appl Supercond 18(2):560–563. https://doi.org/10.1109/Tasc.2008.922510

[27] Davy C, Kalu P, Shen T, Alexander D, Schwarz R, Han K (2005) Fabrication and Characterization of Nanostructured CuAg (Ag-40at% Cu). Microsc Microanal 11(S02):1718. https://doi.org/10.1017/S1431927605509590

[28] Li GM, Liu Y, Su Y, Wang EG, Han K (2013) Influence of high magnetic field on as-cast structure of Cu-25wt%Ag alloys. China Foundry 10(3):162–166. https://doi.org/10.1016/j.cossms.2015.04.002

[29] Zuo XW, Guo R, Zhao CC, Zhang L, Wang EG, Han K (2016) Microstructure and properties of Cu-6wt% Ag composite thermomechanical-processed after directionally solidifying with magnetic field. J Alloy Compd 676:46–53. https://doi.org/10.1016/j.jallcom.2016.03.127

[30] Zuo XW, Han K, Zhao CC, Niu RM, Wang EG (2014) Microstructure and properties of nanostructured Cu28 wt%Ag microcomposite deformed after solidifying under a high magnetic field. Mater Sci Eng Struct Mater Prop Microstruct Process 619:319–327. https://doi.org/10.1016/j.msea.2014.09.070

[31] Zuo XW, Han K, Zhao CC, Niu RM, Wang EG (2015) Precipitation and dissolution of Ag in ageing hypoeutectic alloys. J Alloy Compd 622:69–72. https://doi.org/10.1016/j.jallcom.2014.10.037

[32] Zuo XW, Qu L, Zhao CC, An BL, Wang EG, Niu RM, Xin Y, Lu J, Han K (2016) Nucleation and growth of gamma-Fe precipitate in Cu-2% Fe alloy aged under high magnetic field. J Alloy Compd 662:355–360. https://doi.org/10.1016/j.jallcom.2015.12.046

[33] Zuo XW, Zhao CC, Niu RM, Wang EG, Han K (2015) Microstructural dependence of magnetoresistance in CuAg alloy solidified with high magnetic field. J Mater Process Technol 224:208–212. https://doi.org/10.1016/j.jmatprotec.2015.05.006

[34] Zuo XW, Zhao CC, Wang EG, Zhang L, Han K, He JC (2013) Microstructure evolution of the proeutectic Cu dendrites in diamagnetic Cu-Ag alloys by electromagnetic suppressing convection. J Low Temp Phys 170(5–6):409–417. https://doi.org/10.1007/s10909-012-0743-z

[35] Zhao CC, Zuo XW, Wang EG, Han K (2017) Strength of Cu-28 wt%Ag composite solidified under high magnetic field followed by cold drawing. Met Mater Int 23(2):369–377. https://doi.org/10.1007/s12540-017-6417-2

[36] Zhao CC, Zuo XW, Wang EG, Niu RM, Han K (2016) Simultaneously increasing strength and electrical conductivity in nanostructured Cu-Ag composite. Mater Sci Eng Struct Mater Prop Microstruct Process 652:296–304. https://doi.org/10.1016/j.msea.2015.11.067

[37] Leprince-Wang Y, Han K, Huang Y, Yu-Zhang K (2003) Microstructure in Cu-Nb microcomposites. Mater Sci Eng Struct Mater Prop Microstruct Process 351(1–2):214–223. https://doi.org/10.1016/s0921-5093(02)00855-9

[38] Yu-Zhang K, Embury JD, Han K, Misra A (2008) Transmission electron microscopy investigation of the atomic structure of interfaces in nanoscale Cu-Nb multilayers. Phil Mag 88(17):2559–2567. https://doi.org/10.1080/14786430802380485

[39] Beyerlein IJ, Demkowicz MJ, Misra A, Uberuaga BP (2015) Defect-interface interactions. Prog Mater Sci 74:125–210. https://doi.org/10.1016/j.pmatsci.2015.02.001

[40] Wang J, Misra A (2011) An overview of interface-dominated deformation mechanisms in metallic multilayers. Curr Opin Solid State Mater Sci 15(1):20–28. https://doi.org/10.1016/j.cossms.2010.09.002

[41] Beyerlein IJ, Mara NA, Bhattacharyya D, Alexander DJ, Necker CT (2011) Texture evolution via combined slip and deformation twinning in rolled silver–copper cast eutectic nanocomposite. Int J Plast 27(1):121–146. https://doi.org/10.1016/j.ijplas.2010.05.007

[42] Cui BZ, Xin Y, Han K (2007) Structure and transport properties of nanolaminate Cu-Nb composite foils by a simple fabrication route. Scripta Mater 56(10):879–882. https://doi.org/10.1016/j.scriptamat.2007.01.038

[43] Tian YZ, Wu SD, Zhang ZF, Figueiredo RB, Gao N, Langdon TG (2011) Microstructural evolution and mechanical properties of a two-phase Cu–Ag alloy processed by high-pressure torsion to ultrahigh strains. Acta Mater 59(7):2783–2796. https://doi.org/10.1016/j.actamat.2011.01.017

[44] Saito Y, Utsunomiya H, Tsuji N, Sakai T (1999) Novel ultra-high straining process for bulk materials—development of the accumulative roll-bonding (ARB) process. Acta Mater 47(2):579–583. https://doi.org/10.1016/S1359-6454(98)00365-6

[45] Valiev RZ, Islamgaliev RK, Alexandrov IV (2000) Bulk nanostructured materials from severe plastic deformation. Prog Mater Sci 45(2):103–189. https://doi.org/10.1016/S0079-6425(99)00007-9

[46] Estrin Y, Vinogradov A (2013) Extreme grain refinement by severe plastic deformation: a wealth of challenging science. Acta Mater 61(3):782–817. https://doi.org/10.1016/j.actamat.2012.10.038

[47] Han K, Embury JD, Petrovic JJ, Weatherly GC (1998) Microstructural aspects of Cu-Ag produced by the Taylor wire method. Acta Mater 46(13):4691–4699. https://doi.org/10.1016/S1359-6454(98)00135-9

[48] Han K, Walsh RP, Ishmaku A, Toplosky V, Brandao L, Embury JD (2004) High strength and high electrical conductivity bulk Cu. Phil Mag 84(34):3705–3716. https://doi.org/10.1080/14786430412331293496

[49] Sun LX, Tao NR, Lu K (2015) A high strength and high electrical conductivity bulk CuCrZr alloy with nanotwins. Scripta Mater 99:73–76. https://doi.org/10.1016/j.scriptamat.2014.11.032

[50] Islamgaliev RK, Nesterov KM, Bourgon J, Champion Y, Valiev RZ (2014) Nanostructured Cu–Cr alloy with high strength and electrical conductivity. J Appl Phys. https://doi.org/10.1063/1.4874655

[51] Beyerlein IJ, Mara NA, Wang J, Carpenter JS, Zheng SJ, Han WZ, Zhang RF, Kang K, Nizolek T, Pollock TM (2012) Structure–property–functionality of bimetal interfaces. JOM 64(10):1192–1207. https://doi.org/10.1007/s11837-012-0431-0

[52] Nizolek T, Mara NA, Beyerlein IJ, Avallone JT, Scott JE, Pollock TM (2014) Processing and deformation behavior of Bulk Cu–Nb nanolaminates. Metallogr Microstruct Anal 3(6):470–476. https://doi.org/10.1007/s13632-014-0172-2

[53] Lu L, Shen Y, Chen X, Qian L, Lu K (2004) Ultrahigh strength and high electrical conductivity in copper. Science 304(5669):422–426. https://doi.org/10.1126/science.1092905

[54] Niu R, Han K (2013) Strain hardening and softening in nanotwinned Cu. Scripta Mater 68(12):960–963. https://doi.org/10.1016/j.scriptamat.2013.02.051

[55] Niu R, Han K, Su Y-F, Besara T, Siegrist TM, Zuo X (2016) Influence of grain boundary characteristics on thermal stability in nanotwinned copper. Sci Rep 6:31410–31410. https://doi.org/10.1038/srep31410

[56] Mishin OV, Godfrey A (2008) Microstructure of ECAE-processed copper after long-term room-temperature storage. Metall Mater Trans A 39(12):2923–2930. https://doi.org/10.1007/s11661-008-9658-3

[57] Eftink BP, Li A, Szlufarska I, Mara NA, Robertson IM (2017) Deformation response of AgCu interfaces investigated by in situ and ex situ TEM straining and MD simulations. Acta Mater 138:212–223. https://doi.org/10.1016/j.actamat.2017.07.051

[58] Eftink BP, Mara NA, Kingstedt OT, Safarik D, Wang S, Lambros J, Robertson IM (2018) Deformation response of cube-on-cube and non-coherent twin interfaces in AgCu eutectic under dynamic plastic compression. Mater Sci Eng, A 712:313–324. https://doi.org/10.1016/j.msea.2017.11.108

[59] Eftink BP, Mara NA, Kingstedt OT, Safarik DJ, Lambros J, Robertson IM (2014) Anomalous deformation twinning in coarse-grained Cu in Ag60Cu40 composites under high strain-rate compressive loading. Mater Sci Eng, A 618:254–261. https://doi.org/10.1016/j.msea.2014.08.082

[60] Han K, Goddard R, Niu R, Li T, Nguyen DN, Michel JR, Lu J, Pantsyrny V (2016) Bending behavior of high-strength conductor. IEEE Trans Appl Supercond 26(4):1–4. https://doi.org/10.1109/TASC.2016.2517412

[61] Goddard RE, Han KH, Nguyen DN (2016) Relative strain in Cu-Nb composite wound wire. Microsc Microanal S3:1992–1993. https://doi.org/10.1017/S1431927616010801

[62] Williams PL, Mishin Y, Hamilton JC (2006) An embedded-atom potential for the Cu–Ag system. Modell Simul Mater Sci Eng 14(5):817–833. https://doi.org/10.1088/0965-0393/14/5/002

[63] Stukowski A (2009) Visualization and analysis of atomistic simulation data with OVITO–the open visualization tool. Modell Simul Mater Sci Eng 18(1):015012–6. https://doi.org/10.1088/0965-0393/18/1/015012

[64] Han K, Lawson AC, Wood JT, Embury JD, Von Dreele RB, Richardson JW (2004) Internal stresses in cold-deformed Cu–Ag and Cu–Nb wires. Philos Magaz 84(24):2579–2593. https://doi.org/10.1080/14786430410001689981

[65] Datsko J, Yang CT (1960) Correlation of bendability of materials with their tensile properties. J Eng Indus 82(4):309–313. https://doi.org/10.1115/1.3664236

[66] Labossiere PE (2007). https://courses.washington.edu/me354a/chap3.pdf. Accessed 03 May 2019

[67] Han K, Hirth JP, Embury JD (2001) Modeling the formation of twins and stacking faults in the ag–cu system. Acta Mater 49(9):1537–1540. https://doi.org/10.1016/S1359-6454(01)00057-X

[68] Hong SI, Hill MA (1998) Microstructural stability and mechanical response of Cu–Ag microcomposite wires. Acta Mater 46(12):4111–4122. https://doi.org/10.1016/S1359-6454(98)00106-2

[69] Dubois JB, Thilly L, Lecouturier F, Olier P, Renault PO (2012) Cu/Nb nanocomposite wires processed by severe plastic deformation for applications in high pulsed magnets: effects of the multi-scale microstructure on the mechanical properties. IEEE Trans Appl Supercond 22(3):6900104–6900104. https://doi.org/10.1109/TASC.2011.2174574

[70] Wilde G, Divinski S (2019) Grain boundaries and diffusion phenomena in severely deformed materials. Mater Trans 60(7):1302–1315. https://doi.org/10.2320/matertrans.MF201934

[71] Divinski SV, Reglitz G, Rösner H, Estrin Y, Wilde G (2011) Ultra-fast diffusion channels in pure Ni severely deformed by equal-channel angular pressing. Acta Mater 59(5):1974–1985. https://doi.org/10.1016/j.actamat.2010.11.063

[72] Wang ZB, Divinski SV, Luo ZP, Buranova Y, Wilde G, Lu K (2017) Revealing interfacial diffusion kinetics in ultra-fine-laminated Ni with low-angle grain boundaries. Mater Res Lett 5(8):577–583. https://doi.org/10.1080/21663831.2017.1368036

[73] Bailey JE, Hirsch PB (1962) The recrystallization process in some polycrystalline metals. Proc R Soc Lond A 267(1328):11–30. https://doi.org/10.1098/rspa.1962.0080

[74] Pravoverov NL, Tribunskaya IA (1969) Initial recrystallization temperature of sintered silver-transition metal composites. Soviet Powder Metall Metal Ceram 8(12):1006–1011. https://doi.org/10.1007/BF00802031

[75] Humphreys FJ, Hatherly M (2004) The Deformed State. In: Humphreys FJ, Hatherly M (eds) Recrystallization and related annealing phenomena, vol 2. Elsevier, Oxford, p 11-II

[76] Hoffman RE, Turnbull D (1951) Lattice and grain boundary self-diffusion in silver. J Appl Phys 22(5):634–639. https://doi.org/10.1063/1.1700085

[77] Sommer J, Herzig C (1992) Direct determination of grain-boundary and dislocation self-diffusion coefficients in silver from experiments in type-C kinetics. J Appl Phys 72(7):2758–2766. https://doi.org/10.1063/1.352328

[78] Hong SI, Hill MA, Sakai Y, Wood JT, Embury JD (1995) On the stability of cold drawn, two-phase wires. Acta Metall Mater 43(9):3313–3323. https://doi.org/10.1016/0956-7151(95)00050-6

[79] Hong SI, Hill MA (1999) Mechanical stability and electrical conductivity of Cu–Ag filamentary microcomposites. Mater Sci Eng, A 264(1):151–158. https://doi.org/10.1016/S0921-5093(98)01097-1

[80] Mote VD, Purushotham Y, Dole BN (2012) Williamson-Hall analysis in estimation of lattice strain in nanometer-sized ZnO particles. J Theor Appl Phys 6(1):6. https://doi.org/10.1186/2251-7235-6-6

[81] Attfield M, Barnes P, Cockcroft JK, Driessen H Determination of Size and Strain. https://pd.chem.ucl.ac.uk/pdnn/peaks/sizedet.htm. Accessed 09 March 2019